Marine Chemistry 210 (2019) 61–71

Contents lists available at ScienceDirect

Marine Chemistry

journal homepage: www.elsevier.com/locate/marchem

Kinetic and equilibrium fractionation of O_2 isotopologues during air-water gas transfer and implications for tracing oxygen cycling in the ocean

Boda Li[a,*], Laurence Y. Yeung[a], Huanting Hu[a,b], Jeanine L. Ash[a]

[a] Department of Earth, Environmental and Planetary Sciences, Rice University, Houston, TX 77005, USA
[b] School of Oceanology, Shanghai Jiao Tong University, Shanghai 200240, China

A B S T R A C T

Oxygen isotopologues are useful tools for understanding biogeochemical processes and chemical budgets in the ocean. For example, the triple-oxygen isotope composition of dissolved oxygen in the ocean mixed layer (i.e., its $\delta^{17}O$ and $\delta^{18}O$ values) is widely used to estimate gross oxygen productivity (GOP), a quantity closely related to gross primary productivity. While recent work has demonstrated the importance of upwelling and horizontal transport to these estimates, the isotopic effects of gas exchange when the mixed layer is out of solubility equilibrium have only been measured for $^{18}O/^{16}O$. Oxygen is rarely at 100% saturation in the surface ocean, so most regions experience net ingassing or outgassing; kinetic fractionation across the air-water boundary is therefore expected to be important. Here, we present the results of air-water gas transfer experiments designed to obtain the kinetic and equilibrium fractionation factors for the four rare O_2 isotopologues $^{16}O^{17}O$, $^{16}O^{18}O$, $^{17}O^{18}O$, and $^{18}O^{18}O$ relative to $^{16}O^{16}O$. Furthermore, we examine their potential effects on isotopologue-based GOP estimates and connect the observed air-water kinetic fractionation factors to dissolved-phase diffusive isotopic fractionation. These kinetic fractionation effects may provide additional constraints on O_2 cycling at the surface and in the deep ocean.

1. Introduction

One of the fundamental challenges in oceanography is understanding the distribution and cycling of O_2. The concentration of O_2 in the ocean is influenced by oceanic food webs (Stramma et al., 2012), biogeochemical cycles (Froelich et al., 1979; Gruber and Sarmiento, 1997), and it provides constraints on the efficiency of the biological "pump" mediating the sequestration of carbon in the deep ocean (Devol and Hartnett, 2001; Honjo et al., 2008; Buesseler and Boyd, 2009). Physical, biochemical, and abiotic chemical processes are all important components of the oceanic oxygen budget, but determining the relative importance of each mechanism in different environments can be challenging. Indirect tracers such as the concentrations of nutrients (e.g., nitrate and phosphate) are closely related to O_2 when biologically cycled, so they may offer some information on oxygen cycling (Bianchi et al., 2018). Radiometric tracers such as ^{14}C, which are used to calculated apparent oxygen utilization rates, cannot distinguish large-scale mixing and transport from diffusion. Oxygen isotopologues occupy a unique niche for these studies because they are direct tracers of biogeochemical cycling, mixing, and diffusion (Bender, 1990; Luz and Barkan, 2000; Levine et al., 2009). However, isotopic fractionation during these processes has not been fully characterized. In this paper, we will focus on the isotopic systematics of molecular diffusion.

At the air-water boundary, molecular diffusion is the rate-limiting step for the dissolution of sparingly soluble gases (e.g. O_2, Ar, N_2, etc.) (Jähne and Haußecker, 1998). In the ocean interior, molecular diffusion can limit oxygen transport to sediments, particles, and micro- and macrofauna. Kinetic isotope fractionation occurs during these processes, but experimental and theoretical studies suggest that the mass, size and shape of the diffusing species are all important determinants of their fractionation factors (Knox et al., 1992; Richter et al., 2006; Bourg and Sposito, 2008; Tempest and Emerson, 2013). Few studies have focused on the isotope effects of O_2 diffusion. The only study to date, by Knox et al. (1992), determined a small $^{18}O/^{16}O$ fractionation factor of 0.9972 for O_2 transfer across the air-water boundary. It was used to support $\delta^{18}O$-based estimates of primary productivity (Quay et al., 1993) and to illustrate how diffusion did not follow a simple gas-kinetic mass dependence (i.e., scaling with the inverse-square-root of the molecular mass).

Understanding multi-isotope systematics has since become important for oceanography, renewing interest in the mass dependence of diffusion for O_2. In situ estimates of primary productivity—or, more precisely, gross oxygen productivity (GOP)—have relied on the simultaneous mass balance of multiple O_2 isotopologues in the mixed layer. Using a multiple O_2-isotopologue mass balance mitigates some of the key uncertainties of bottle incubations and in situ $^{18}O/^{16}O$-isotope based approaches to primary productivity (Juranek and Quay, 2005, 2013; Quay et al., 2010); thus it has been adopted widely in studies of

* Corresponding author.
E-mail address: bl21@rice.edu (B. Li).

https://doi.org/10.1016/j.marchem.2019.02.006
Received 18 June 2018; Received in revised form 12 February 2019; Accepted 19 February 2019
Available online 21 February 2019
0304-4203/

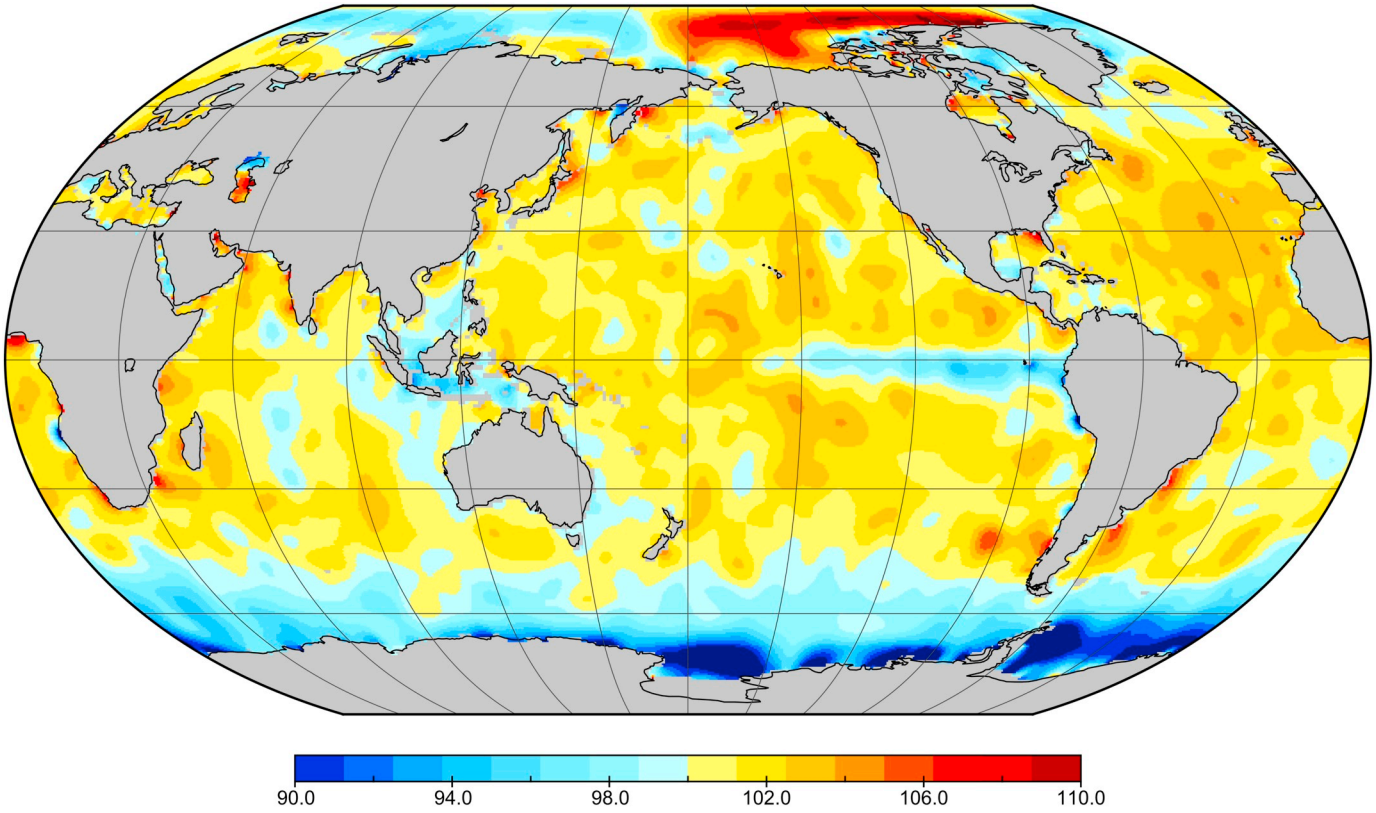

Fig. 1. Annual-mean dissolved oxygen saturation (%) in the surface oceans in 2013. Data from (Garcia et al., 2014).

the carbon budget of the surface ocean. In particular, the multi-isotopologue approach has proven useful for determining the carbon export efficiency in the surface ocean (i.e., the net-to-gross oxygen production ratio) when paired with O_2/Ar ratio measurements (Luz and Barkan, 2000, 2005; Bender, 2000; Juranek and Quay, 2013). While methodological improvements have refined the fluxes used in surface O_2 budgets (Kaiser, 2011; Prokopenko et al., 2011; Luz and Barkan, 2011; Nicholson et al., 2012; Manning et al., 2017), uncertainties in the approach related to physical fractionation have persisted. For example, the kinetic isotopic effects due to gas exchange are only known for $^{18}O/^{16}O$. Yet, large regions of the global ocean are out of solubility equilibrium with respect to O_2 (Fig. 1), resulting in net outgassing or ingassing at steady state that could bias estimates of GOP due to kinetic isotope fractionation of O_2 isotopologues (Kaiser, 2011). Moreover, much of the surface ocean is characterized by low productivity. In oligotrophic regions in particular, factors that might otherwise be minor such as gas exchange and bubble injection could become important, leading to biases in the interpretation of small O_2 signals if such processes are not considered explicitly.

In this paper, we evaluate the importance of non-equilibrium gas exchange on the isotopologue budgets of dissolved O_2. We conducted new measurements of the kinetic and equilibrium isotope fractionation for O_2 transfer through the air-water interface, for both the singly-substituted ($^{16}O^{17}O$ and $^{16}O^{18}O$) and multiply-substituted rare isotopologues ($^{17}O^{18}O$ and $^{18}O^{18}O$) of O_2. An earlier experiment had suggested that air-water gas exchange may exhibit an unusual mass dependence, one that concentrates $^{18}O^{18}O$ in the gas phase much more than expected (Yeung et al., 2015). Our experiments test this hypothesis directly, free from the biological cycling that complicated the previous experiment. In addition, simultaneous measurements of five O_2 isotopologues ($^{16}O^{16}O$, $^{16}O^{17}O$, $^{16}O^{18}O$, $^{17}O^{18}O$, and $^{18}O^{18}O$) provide an opportunity to examine the mass dependence of gas exchange and diffusion in the aqueous phase.

2. Methods

Kinetic fractionation factors were measured for O_2 diffusion into water following the methodology of Knox et al. (1992) and Tempest and Emerson (2013). The experiment progressed as follows: We introduced O_2 into the headspace of a closed system that contained degassed, deionized water. As the O_2 dissolved into the water, changes in the volume and isotopic composition of O_2 in the headspace were monitored. Equilibrium air-water isotopologue fractionations were also measured in a separate set of experiments. By fitting a forward model of the headspace evolution to the isotopic data—from solubility disequilibrium to solubility equilibrium—we obtained kinetic fractionation factors for four rare O_2 isotopologues ($^{16}O^{17}O$, $^{16}O^{18}O$, $^{17}O^{18}O$, and $^{18}O^{18}O$) simultaneously during O_2 dissolution.

2.1. Experiments

2.1.1. Air-water equilibration

Bottles for dissolved-gas sampling (1 L) were prepared according to established methods (Reuer et al., 2007): First, they were washed with phosphate-free detergent (Liquinox) and then triple-rinsed with distilled water. After the flasks were dried, they were poisoned with 200 μL saturated $HgCl_2$ solution, and dried at 40–45 °C. Calculated concentrations of $HgCl_2$ after introducing a water sample into the flasks are 30–50 μg mL^{-1}, more than the 20 μg mL^{-1} recommended by Kirkwood (1992) to halt biological activity. Finally, all flasks were evacuated on a turbo-pumped high-vacuum line to $\leq 1 \times 10^{-3}$ mbar through a Louwers-Hapert high-vacuum valve. The side arm of the valve on each bottle was filled with distilled water to reduce atmospheric contaminants during storage and sampling.

Laboratory air was equilibrated with distilled water at 25.0 °C by shaking a covered 5 L beaker containing 3 L of water on an orbital shaker (110 rpm) for 48–96 h. To facilitate air-water gas exchange, the shaking direction was reversed every minute during this time period.

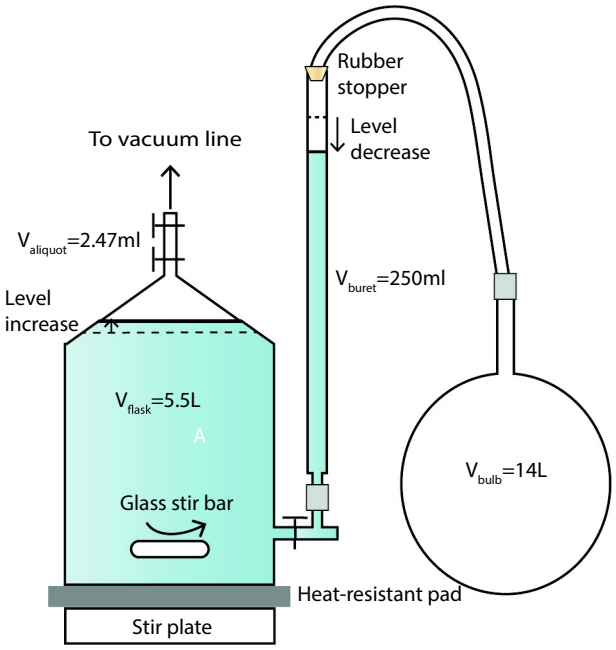

Fig. 2. Schematic diagram of the gas-exchange experiment. During an experiment, the water level in the buret drops, and the water level in the Kimax flask rises, as O_2 gas dissolves from the flask headspace into the water.

Water samples (300–500 mL) were then extracted into evacuated sample flasks, which were pre-poisoned with $HgCl_2$. After shaking for > 48 h, the residual gas in the drained bottles was collected onto silica gel fingers at −196 °C for 45 min. The sample flasks were kept at −30 °C to −40 °C during the gas transfer to limit the transfer of residual water and $HgCl_2$ into the vacuum system. The gases were further dried and CO_2 removed by passing them through two U-shaped traps at −196 °C upstream of the silica gel sample finger.

2.1.2. Kinetic gas transfer

Three kinetic gas-transfer experiments were conducted using a closed, modified 5.53 ± 0.04 L Kimax flask system (Fig. 2). Gas exchange and headspace sampling took place in the Kimax flask, which is filled with degassed, deionized water. All the water in the system was first deionized on a Millipore system (18.2 MΩ·cm) and then passed through an additional sterilizing filter (0.22 μm). The water was then degassed by boiling for 2 h. The boiled water was immediately transferred to the Kimax flask and isolated using a high-vacuum Louwers-Hapert valve while minimizing headspace volume. It was then cooled to room temperature. A buret was connected to the flask through an Ultra-Torr connection with the valve that was attached to the side of the flask. Degassed water was later added to the buret; an unavoidable, but small, amount of air contamination was associated with this step (< 5% of the total dissolved O_2 in the Kimax flask at the end of the experiment; see Section 3.4 for further discussion). The top of the buret was connected to a 14.0 ± 0.3 L gas bulb filled with air, which acts as a ballast volume to sustain a stable atmospheric pressure during the experiment. It isolates the system from barometric fluctuations that may affect the headspace pressure during the experiment. The headspace gas was sampled at various times during the experiment by expanding the headspace gas into the volume between the two valves at the top of the flask. The aliquot volume was 2.47 ± 0.27 mL (102.0 ± 11.5 μmol O_2 at 1 atm pure O_2).

The experiment was conducted at room temperature (22 ± 1 °C) without active temperature stabilization. No significant temperature dependence for the $^{18}O/^{16}O$ kinetic fractionation factor for O_2 has been observed between 10 °C and 20 °C (Knox et al., 1992). Before each experiment, the headspace pressure was pumped until it reached a pressure equal to the vapor pressure of water (24.9 ± 1.6 mbar at room temperature). Next, we opened the valve on the side of the flask to allow water to flow between the buret and the Kimax flask, which balanced the pressure in the headspace. The experiment was initiated upon introducing pure O_2 (ultra-high purity; 99.9999%) into the headspace of the water flask. As O_2 dissolves into the water, the headspace pressure in the main volume decreases, drawing in water from the buret. The volume change observed at the buret is thus used to determine the volume of O_2 dissolved in the water (after accounting for the change in hydrostatic pressure). The headspace was sampled at intervals corresponding to a 5% to 15% change in O_2 saturation. Two types of glass stir bars (lengths 4.5 ± 0.1 cm, 2.3 ± 0.1 cm) were used to mix the water in the flask at different rates while limiting visible perturbations to the air-water interface.

Prior to isotopic analysis, each headspace O_2 aliquot was transferred to a silica gel finger held at −196 °C for 15 min. Water and other condensable gases were removed cryogenically through two U-traps held at −196 °C by liquid nitrogen. The sampled O_2 was purified according to methods described previously using an Agilent 7890B Gas Chromatograph (GC) held at −80 °C (Yeung et al., 2018). Samples were then analyzed on a modified, high-resolution *Nu* Instruments *Perspective IS* isotope ratio mass spectrometer (IRMS) in dual-inlet mode according to established techniques (Yeung et al., 2016). Long-term external precision for $\delta^{18}O$, $^{17}\Delta$, Δ_{35}, and Δ_{36} values is ± 0.025‰, ± 3 ppm, ± 0.12‰, and ± 0.04‰, respectively (1σ), based on replicate analyses of atmospheric O_2.

2.2. Isotopic terminology

The $^{33}O_2/^{32}O_2$, $^{34}O_2/^{32}O_2$, $^{35}O_2/^{32}O_2$, and $^{36}O_2/^{32}O_2$ ratios measured on the mass spectrometer are reported as $\delta^{18}O$ values for $^{18}O/^{16}O$ ratios (Eq. (1)), $^{17}\Delta$ values for triple-oxygen composition (Eq. (2)), and Δ_{35} and Δ_{36} values for clumped-isotope composition (Eqs. (3)–(6)).

$$\delta^{18}O = \left(\frac{^{18}R_{Sample}}{^{18}R_{WG}} - 1\right) \times 1000‰ \quad (1)$$

$$^{17}\Delta = \ln\frac{^{17}R_{Sample}}{^{17}R_{WG}} - 0.518 \times \ln\frac{^{18}R_{Sample}}{^{18}R_{WG}} \quad (2)$$

$$\Delta_{36} = \left(\frac{^{36}R_{Sample}}{^{36}R_{Stochastic}} - 1\right) \times 1000‰ \quad (3)$$

$$\Delta_{35} = \left(\frac{^{35}R_{Sample}}{^{35}R_{Stochastic}} - 1\right) \times 1000‰ \quad (4)$$

$$^{36}R_{stochastic} = {}^{18}R^2 \quad (5)$$

$$^{35}R_{stochastic} = 2\,{}^{17}R\,{}^{18}R \quad (6)$$

here, R refers to the ratio of relative concentration of a specific isotope or isotopologue to the most abundant isotope or isotopologue. For example, ^{18}R refers to the ^{18}O mole concentration divided by the mole concentration of most abundant isotope ^{16}O, while for ^{36}R refers to the $^{18}O^{18}O$ mole concentration divided by the mole concentration of most abundant isotopologue $^{16}O^{16}O$. In Eq. (6), a factor of two is included for $^{35}R_{stochastic}$ because both $^{18}O^{17}O$ and $^{17}O^{18}O$ molecules have cardinal mass 35. The subscript WG refers to working gas, which is the starting gas of the experiment. The $^{17}\Delta$ value describes the "excess" ^{17}O relative to an expected abundance of ^{17}O, based on the $\delta^{18}O$ value (Young et al., 2002). We choose a reference slope of 0.518, which is most relevant to oceanographic applications (Luz and Barkan, 2005). The clumped-isotope distribution in O_2 is reported as Δ_{36} and Δ_{35} values, which quantify the excess in $^{18}O^{18}O$ and $^{17}O^{18}O$, respectively, relative to the stochastic distribution of isotopes in O_2. The $\delta^{18}O$ and $^{17}\Delta$ values in this study quantify the changes in bulk isotopic composition of the O_2, expressed

in parts per thousand (‰) and parts-per-million (ppm), respectively. The Δ_{35} and Δ_{36} values are absolute clumped-isotope excesses or deficits reported in parts per thousand (‰).

The gas exchange experiment involves both kinetic and equilibrium fractionation processes, which will be defined and related to δ/Δ terminology below. Kinetic fractionation of O_2 isotopologues occurs when they diffuse into or out of water; the magnitude of the fractionation reflects the relative diffusion rates across the air-water boundary for different isotopologues. Equilibrium fractionation occurs when ingassing and outgassing of O_2 is equal. Differences in free energy for different O_2 isotopologues dissolved in water lead to small fractionations typically < 1‰ at 25 °C at equilibrium (Benson and Krause, 1984). The equilibrium isotopic fractionation factor, α_{eq}, is defined as:

$$\alpha_{eq} = \frac{(H/L)_d}{(H/L)_g} = \frac{H_d/H_g}{L_d/L_g} = \frac{\gamma_H}{\gamma_L} \quad (7)$$

here, H represents the concentration of heavy isotopologues ($^{16}O^{17}O$, $^{16}O^{18}O$, $^{17}O^{18}O$, or $^{18}O^{18}O$) and L represents the concentration of $^{16}O^{16}O$. The subscripts d and g represent the dissolved and gas phase, respectively. Note that α_{eq} can also be represented as the ratio of the Henry's law constants, γ_H/γ_L.

Benson and Krause (1984) determined the equilibrium fractionation for $^{16}O^{18}O$ ($^{18}\alpha_{eq}$) to be 1.00072 at 22 °C, which is not sensitive to temperature changes around room temperature. For example, the equilibrium fractionation for $^{16}O^{18}O$ ($^{18}\alpha_{eq}$) changes from 1.00073 to 1.00071 between 20 °C and 24 °C. Over this range, the change in $\delta^{18}O$ at equilibrium would not be detectable. The equilibrium fractionation factor for $^{16}O^{17}O$ is inferred to be 1.00038 between 20 °C and 24 °C, constrained by mass-dependent fractionation, based on previous triple-oxygen measurements (Reuer et al., 2007; Stanley et al., 2010; Nicholson et al., 2012; Palevsky et al., 2016).

Previous work suggests that the gas transfer coefficient has a power-law dependence on the Schmidt number (*Sc*) of the gas in the fluid (Jähne and Haußecker, 1998). The Schmidt number is the kinematic viscosity of the fluid (ν, in this case for water) divided by the molecular diffusivity of the gas in the dissolved phase (D); thus, the gas transfer coefficient can be rewritten as:

$$k = B \times Sc^{-n} = B(\nu/D)^{-n} \quad (8)$$

where the coefficient B depends on physical parameters such as the boundary-layer thickness and mixing rate, and -n is power-law exponent. Different isotopologues share the same B value during gas transfer because of the same physical conditions.

The kinetic fractionation factor for gas transfer α_k is defined as k_H/k_L, the ratio of gas transfer flux between different species under the same concentration gradient:

$$\alpha_k = \frac{k_H}{k_L} \quad (9)$$

Because different isotopic species share the same B value and kinematic viscosity, α_k can be simply related to the ratio of aqueous diffusion coefficients of different isotopologues (D_H/D_L):

$$\alpha_k = \left(\frac{D_H}{D_L}\right)^n = \alpha_D{}^n \quad (10)$$

The value of n varies between 1/2 and 2/3 depending on the roughness of the air-water interface, with $n = 1/2$ describing rough surfaces and $n = 2/3$ describing the limit of a perfectly smooth surface (Jähne and Haußecker, 1998). Kinetic isotopologue fractionation across the air-water interface can therefore be used to constrain isotopologue fractionation during aqueous-phase diffusion as well. We will discuss this application in detail in the section 4.4.

One can also define terms that characterize mass-dependent fractionation for this process. The triple-oxygen term $\theta_{17/18}$ is defined here as (Angert et al., 2003):

$$\theta_{17/18} \approx \theta_{33/34} = \frac{\ln {}^{33}\alpha_k}{\ln {}^{34}\alpha_k} \quad (11)$$

Values of $\theta_{17/18}$ are close to 0.5 for most processes because the mass difference between $^{16}O^{17}O$ and $^{16}O^{16}O$ is roughly half that between $^{16}O^{18}O$ and $^{16}O^{16}O$ (Young et al., 2002; Angert et al., 2003; Helman, 2005). Similarly, θ values for isotopically "clumped" species ($^{18}O^{18}O$ and $^{17}O^{18}O$) can be defined:

$$\theta_{36/34} = \frac{\ln {}^{36}\alpha_k}{\ln {}^{34}\alpha_k} \quad (12)$$

$$\theta_{35/34} = \frac{\ln {}^{35}\alpha_k}{\ln {}^{34}\alpha_k} \quad (13)$$

Here, a value for $\theta_{36/34}$ of 2 and $\theta_{35/34}$ of $1 + \theta_{17/18}$ would preserve Δ_{36} and Δ_{35} values upon fractionation (Yeung et al., 2012). Higher values of $\theta_{36/34}$ and $\theta_{35/34}$ relative to those specified above would yield increases in Δ_{36} and Δ_{35} values, while lower values of $\theta_{36/34}$ and $\theta_{35/34}$ relative to those specified above would yield decreases in Δ_{36} and Δ_{35} values.

2.3. Model of the gas-exchange experiment

To model the kinetic component of the gas-transfer process, one must derive an expression for the fluxes of O_2 isotopologues across the air-water interface. Net O_2 fluxes *F* depend on a transfer coefficient (k) and the concentration gradient (ΔC) across the interface:

$$F = k \times \Delta C \quad (14)$$

Following Knox et al. (1992) and Tempest and Emerson (2013), we express Eq. (14) in terms of the O_2 partial pressure P, its Henry's law constant γ, and the concentration of O_2 in the dissolved phase c_d:

$$\frac{dC_d}{dt} = k(P\gamma - c_d) \quad (15)$$

The Henry's law constant of O_2 can be calculated from its solubility at air partial pressure (Garcia and Gordon, 1992). The term ($P\gamma$-c_d) represents the "concentration gradient" across the air-water boundary when out of solubility equilibrium.

Because $^{16}O^{16}O$ occupies > 99.5% of the total oxygen budget, we assume that the volumetric change in O_2 measured at the buret is equal to the change in $^{16}O^{16}O$. This assumption results in a < 0.5% error, which is negligible. Using this assumption, the net flux of $^{16}O^{16}O$ across the air-water interface is expressed as a change in its concentration in the dissolved phase (L_d):

$$\frac{dL_d}{dt} = k_L(P\gamma_L - L_d) \quad (16)$$

L_d equals to the mole number of $^{16}O^{16}O$ divided by the volume of water (V) in the flask. A similar expression can be derived for the heavy isotopologues ($^{16}O^{17}O$, $^{16}O^{18}O$, $^{17}O^{18}O$, and $^{18}O^{18}O$) in the dissolved phase (H_d):

$$\frac{dH_d}{dt} = k_H\left[P * \left(\frac{H}{L}\right)_g * \gamma_H - H_d\right] \quad (17)$$

where each isotopologue has its own Henry's law constant and a partial pressure corresponding to its abundance in the gas phase.

Mass balance connects the dissolved phase and the gas phase because the headspace-water system can be treated as a closed system. The isotopic composition of the headspace gas [i.e., $(H/L)_g$] at any point in time is therefore related to the isotopic composition of the initial headspace gas and the concurrent dissolved gas via Eq. (18):

$$\left(\frac{H}{L}\right)_g = \frac{V_{gi}H_i - VH_d}{V_{gi}L_i - VL_d} \quad (18)$$

In Eq. (18), V_{gi}, H_i, and L_i represent the initial head space volume, gas-

phase heavy-isotopologue concentration, and light-isotopologue concentration, respectively. V, H_d, and L_d correspond to the water volume, dissolved heavy-isotopologue concentration, and dissolved light-isotopologue concentration at time t. By substituting $(H/L)_g$ (Eq. (18)), k_H (Eq. (9)) and γ_H (Eq. (7)) into Eq. (17) we arrive at:

$$\frac{dH_d}{dt} = k_L\alpha_k\left(P * \frac{V_{gi}H_i - VH_d}{V_{gi}L_i - VL_d} * \gamma_L * \alpha_{eq} - H_d\right) \quad (19)$$

The k_L value is calculated from the temporal evolution of the buret water level, while the other variables are known, measured, or inferred (see below). The model can be stepped in a forward direction using Eqs. (16) and (19) starting with known isotopologue compositions at time $t = 0$ to calculate the temporal evolution of the headspace O_2 isotopologue composition.

Our model inherits most of the notation and expressions used in Knox et al. (1992). Kaiser (2011) derived a slightly different model, defining separate evasion (outgassing) and invasion (ingassing) kinetic fractionation factors:

$$c\frac{d\delta}{dt} = k_L[c_{sat}(\varepsilon_I - \delta) - c\varepsilon_E(1 + \delta)] \quad (20)$$

The evasion kinetic fractionation factor $(1 + \varepsilon_E)$ in Eq. (20) is the same as α_k in Eq. (19), while the invasion kinetic fractionation factor $(1 + \varepsilon_I)$ is equal to the product of the kinetic and equilibrium fractionation factors $\alpha_k \times \alpha_{eq}$.

Note that over the course of the gas exchange experiment, the falling water level in the buret causes the flask's headspace pressure P to decrease. This pressure drop arises from an increase in the ballast volume (the volume above the headspace of the buret in Fig. 2) and a decrease in the hydrostatic pressure ($\Delta P_{hydrostatic}$). The former accounts for about one-third of the excess pressure drop and the latter accounts for the remaining two-thirds. Both of these effects are included in the calculation of the flask headspace pressure according to Eq. (21),

$$P = P_i - \Delta P_{hydrostatic} - \Delta P_{ballast} = P_i - \rho g\Delta h - P_{atm}\frac{\Delta V}{V_{bulb} + \Delta V} \quad (21)$$

where P_i is the initial headspace pressure of water flask, $\Delta P_{ballast}$ is the pressure change in the ballast volume caused by the volume change ΔV, ρ is the density of water, g is the acceleration due to gravity ($9.81\ m\ s^{-2}$), and Δh is the drop in water level in the buret relative to that in the flask (it increases over the course of the experiment). The atmospheric pressure (P_{atm}) used here is the average sea-level pressure, 101.325 kPa.

Finally, during the experiment, the volume of the gas in the flask headspace also changes by a volume ΔV_{dis} as the gas dissolves into water:

$$\Delta V_{dis} = V_{gi} - V_g \quad (22)$$

We update this volume change into our forward model at each time step. An ideal gas law is used to calibrate both the volume change and the pressure change in the flask system.

A systematic error may arise from the initial O_2 saturation state of the water in the buret. Although the water was carefully degassed via boiling, air ingassing during buret filling was unavoidable. This ingassing caused a non-zero saturation for the buret water, which enters the flask during the experiment and degasses into the headspace. The potential errors due to this complication will be discussed in the context of the results in Section 3.4.

3. Results

3.1. Air-water equilibration

Measurements of O_2 dissolved in water yielded $\delta^{18}O$ and $^{17}\Delta$ values consistent with previous determinations, i.e., 0.699 ± 0.032‰ and 10 ± 2 ppm (95% confidence intervals, $n = 12$; see Table 1), which suggest that $\theta_{17/18,eq} = 0.528$ (Reuer et al., 2007; Palevsky et al., 2016). The Δ_{36} values may be slightly lower than from those of air, but they are not distinguishable at the 95% confidence level: At 25 °C, we measured clumped-isotope compositions of dissolved O_2 in water of $\Delta_{35} = 0.98 \pm 0.07$‰ and $\Delta_{36} = 1.944 \pm 0.018$‰ (95% CI; $n = 12$) compared to $\Delta_{35} = 1.02 \pm 0.05$‰ and $\Delta_{36} = 1.972 \pm 0.023$‰ (95% CI; $n = 17$) for Houston air measured during the same analytical sessions (Yeung et al., 2016). These values are consistent with equilibrium dissolution fractionating O_2 isotopologues with $\theta_{35/34} = 1 + \theta_{17/18}$ and $\theta_{36/34} = 2.00$. While we cannot rule out $\theta_{36/34,eq} < 2$ at solubility equilibrium, $\theta_{36/34,eq} > 2$ appears unlikely. Neither isotopologue mass law leads to detectable changes in Δ_n values upon dissolution. Based on these results, we will use $\theta_{17/18,eq} = 0.528$, $\theta_{35/34,eq} = 1.528$, and $\theta_{36/34,eq} = 2.00$ to describe the isotopologue fractionation at solubility equilibrium.

Table 1
Isotopic compositions for air dissolved in distilled water at 25 °C.

Sample	$\delta^{18}O$/‰	$^{17}\Delta$/ppm	Δ_{35}/‰	Δ_{36}/‰
1	0.724	9	0.89	1.916
2	0.627	14	0.96	1.992
3	0.620	12	0.93	1.933
4	0.704	4	0.93	1.957
5	0.776	6	0.76	1.961
6	0.717	17	1.02	1.900
7	0.764	5	1.07	1.904
8	0.724	9	0.95	1.970
9	0.727	10	1.05	1.938
10	0.634	10	1.16	1.951
11	0.689	10	1.08	1.937
12	0.680	9	0.92	1.968
Mean ± 1σ	0.699 ± 0.051	10 ± 4	0.98 ± 0.11	1.944 ± 0.028
Mean ± 95% CI	0.699 ± 0.032	10 ± 2	0.98 ± 0.07	1.944 ± 0.018
Air ± 95% CI[a]	0.000 ± 0.016	0 ± 2	1.02 ± 0.05	1.972 ± 0.023

[a] Measured during the same analytical sessions as the experiments.

3.2. k_L value (gas transfer coefficient for $^{16}O^{16}O$)

The k_L value is the rate coefficient describing O_2 dissolution into water. To obtain this value, we first calculated the O_2 saturation state in water over time using observed buret-volume changes, the ideal gas law, the O_2 solubility, and the total volume of water in the flask. Next, we used the solution to Eq. (16), i.e.,

$$L_d = P\gamma_L(1 - e^{-k_L t}) \quad (23)$$

to obtain k_L from an exponential fit to the temporal evolution of dissolved O_2 concentration. The results are shown in Fig. 3. The misfit between some fitted values and experimental data is mainly caused by the variation of temperature during the experiment. Gas transfer rates were modulated by changing the size and rotation rate of the stir bar between experiments.

3.3. Kinetic fractionation factors

Kinetic fractionation factors were determined from the time-evolution of headspace O_2 isotopic compositions. Representative plots of the change in isotopic composition as a function of O_2 saturation are shown in Fig. 4. The results from the other 2 experiments are presented in supplementary materials (Figs. S1 and S2). We fit the experimental data to the model curve (Eqs. (16) and (19)) using a least-squares algorithm to obtain best-fit kinetic fractionation factors and their fitting errors for the minor isotopologues. The results are listed in Table 2.

Fig. 4A shows an increase in $\delta^{18}O$ values of headspace O_2 at the beginning of the experiment, reaching a peak at around 50% or 60% saturation. The precise O_2 saturation state corresponding to the

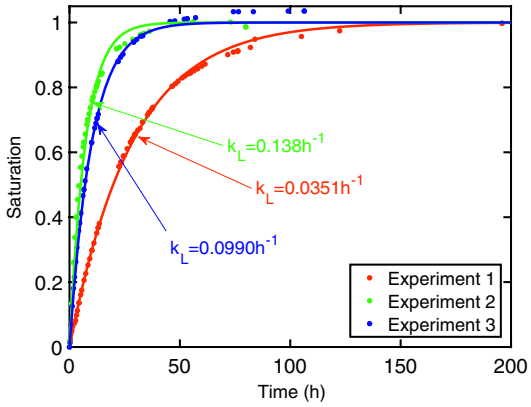

Fig. 3. Oxygen saturation vs. time for all three experiments along with the kinetic gas transfer coefficient of O_2. The uncertainty in the saturation measurements is 0.5%, but the overall uncertainty is larger due to potential temperature fluctuations and inaccuracies in the initial buret-water saturation (see Section 3.4). The k_L values obtained were 0.0351 ± 0.004 h^{-1} (R^2 = 0.999), $0.138^{+0.005}_{-0.006}$ h^{-1} (R^2 = 0.992), and 0.0990 ± 0.003 h^{-1} (R^2 = 0.998) for experiments 1, 2, and 3, respectively, with the uncertainty limits reflecting 95% confidence intervals.

maximum $\delta^{18}O$ value depends on k_L. In general, lighter isotopologues diffuse into water faster than heavy isotopologues, so the residual O_2 in the headspace has a higher proportion of heavy isotopologues during early stages of the experiment. As O_2 builds up in the dissolved phase, the outgassing flux from the dissolved phase increases. The lighter isotopologues outgas preferentially from the dissolved phase, which then lowers the proportion of heavy isotopologues in the headspace. An equilibrium is reached when the outgassing and ingassing rates are equal for all species. The expected equilibrium values of $\delta^{18}O$ are −0.265‰, −0.245‰, and −0.257‰ for Experiments 1, 2, and 3, respectively. We note here that all three experiments showed a lower $\delta^{18}O$ than expected at equilibrium. This deviation is also apparent in the previous experiment by Knox et al. (1992), although it was not discussed; we will address this disparity and its implications in more detail in Section 3.4.

The mean $^{34}\alpha_k$ value derived from the three experiments was 0.9978 ± 0.0004 (1σ). The change in $^{17}\Delta$, Δ_{35}, and Δ_{36} values was small, suggesting a $\theta_{17/18,k} \approx 0.518$, $\theta_{35/34,k} \approx 1 + \theta_{17/18,k} \approx 1.5$, and $\theta_{36/34,k} \approx 2$. We obtained a mean $\theta_{17/18,k}$ value of 0.517 ± 0.002 and a mean $\theta_{36/34,k}$ value of 1.948 ± 0.032 (1σ, n = 3 experiments). The fitting errors for $^{34}\alpha_k$ and $^{33}\alpha_k$ are smaller than the last digits in the values reported in Table 2. To test the veracity of these results, we ran 3000 independent fits for each parameter in each experiment after randomly varying all data points in a normal distribution about the measured values (within the analytical standard deviation, i.e., ± 3 ppm for $^{17}\Delta$ and ± 0.04‰ for Δ_{36}). The means of the probability distributions for these "Monte Carlo" experiments (Fig. 5) yield $\theta_{17/18,k}$ = 0.517 ± 0.003 and $\theta_{36/34,k}$ = 1.948 ± 0.011 (1σ) for the three experiments, which are indistinguishable from the unperturbed best-fit results. Shapiro-Wilk normality tests suggest that the Monte Carlo distributions are quasi-normal: they are indistinguishable from normal when n = 300 (p = 0.08), but distinguishable for n = 3000 ($p < 3 \times 10^{-4}$).

3.4. Main uncertainties

As shown in Fig. 4A, we observed an offset between the modeled and experimental $\delta^{18}O$ value at the end of the experiment (~100% O_2 saturation). This offset may have had four potential origins: air contaminations present at the start of the experiment, air contaminations that accumulated over the course of the experiment, artifacts associated with repeated sampling of the headspace O_2, and artifacts associated with temperature inaccuracy. Below we examine each possibility.

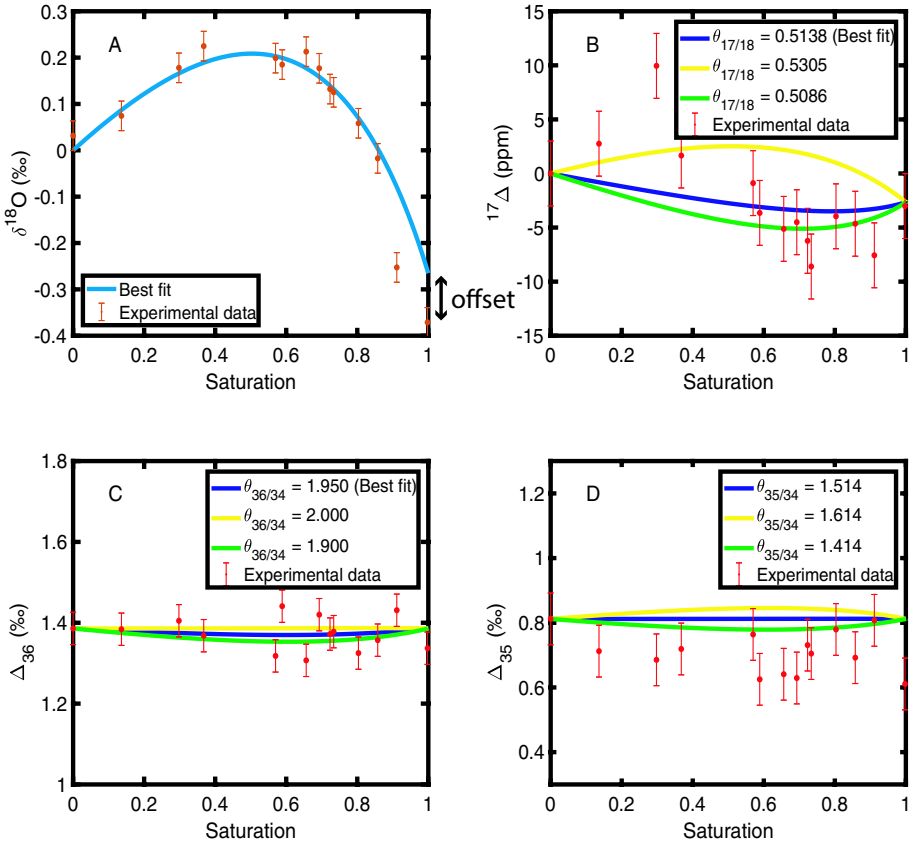

Fig. 4. Representative experimental results for the kinetic gas-transfer experiment. The red points show the measured data points with analytical 1σ error bars and the dark blue line shows the best-fit model result. Values of (A) $\delta^{18}O$, (B) $^{17}\Delta$, (C) Δ_{36}, and (D) Δ_{35} for the headspace O_2 are plotted against dissolved O_2 saturation. In A, near 100% saturation, there is an offset between the modeled and experimental $\delta^{18}O$ value that is discussed in section 3.4. In B, C, and D, the green and yellow lines show sensitivities of the model curve to assumed θ value. In D, a best-fit $\theta_{35/34}$ was not found, so the dark blue line corresponds to a model that assumes $^{35}\alpha_k = {}^{34}\alpha_k{}^{33}\alpha_k$ or $\theta_{35/34} \approx 1 + \theta_{17/18}$. The data for the other two experiments can be found in the supplementary materials. (For interpretation of the references to colour in this figure legend, the reader is referred to the web version of this article.)

Table 2
Best-fit kinetic fractionation factors and θ values for $^{16}O^{17}O$, $^{16}O^{18}O$, and $^{18}O^{18}O$ obtained from gas-exchange experiments.

Experiment	$^{34}\alpha_k$	$^{33}\alpha_k$	$\theta_{17/18,k}$	$\theta_{36/34,k}$
1	0.9974[a]	0.9987[a]	0.514 ± 0.003	1.950 ± 0.043
2	0.9980[a]	0.9990[a]	0.520 ± 0.005	1.936 ± 0.063
3	0.9981[a]	0.9990[a]	0.517 ± 0.004	1.957 ± 0.058
Mean ± 1σ	0.9978 ± 0.0004	0.9989 ± 0.0001	0.517 ± 0.002	1.948 ± 0.032

[a] Fit uncertainties not shown because they are much smaller than the experimental reproducibility.

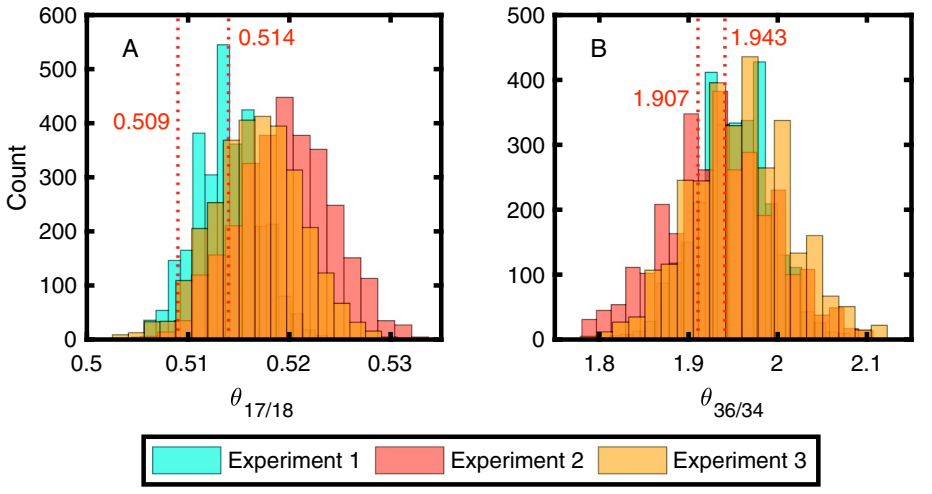

Fig. 5. Histograms of (A) $\theta_{17/18}$ and (B) $\theta_{36/34}$ by the Monte Carlo method ($n = 3000$). The histograms show quasi-normal distributions (see text). The red dotted lines show theoretical $\theta_{17/18}$ and $\theta_{36/34}$ values for pinhole diffusion (0.509 and 1.943, respectively), and O_2-water interdiffusion for one water molecule (0.514 and 1.907, respectively). (For interpretation of the references to colour in this figure legend, the reader is referred to the web version of this article.)

The most likely source of air contamination at the start of the experiment is air dissolved in the buret water; although the water was degassed by boiling, air ingassing during buret filling was unavoidable. Dissolved air in the buret water can outgas into the headspace once it enters the Kimax flask. To estimate the potential effects from this contamination, we use a mass-balance relationship to calculate the isotopic composition of the headspace gas:

$$V_1\delta^{18}O_{air} + V_2\delta^{18}O_{WG} = (V_1 + V_2)\delta^{18}O_{WG\ altered} \quad (24)$$

where V_1 and V_2 represent the volume of buret oxygen and the volume of headspace oxygen, respectively. Here, $\delta^{18}O_{WG} = 0$ and $\delta^{18}O_{air}$ is equal to the ambient atmospheric value of −3.2‰. We estimate the maximum contamination by calculating V_1 assuming 100% air saturation for the buret water based on Henry's law. If V_2 is the initial headspace volume, ~450 mL, we obtain $\delta^{18}O_{WG\ altered} = -0.008‰$, which is not enough to explain the −0.11‰ offset between the expected value and experimental value. To achieve −0.11‰ for $\delta^{18}O_{WG\ altered}$, V_1 needs to be 14.5 mL, which requires 2.4 L of air-saturated water (about 12 times more than observed) to enter the Kimax flask. If V_2 is the final headspace volume, ~250 mL, we obtain $\delta^{18}O_{WG\ altered} = -0.015‰$, which is still not enough to explain the −0.11‰ difference. Another potential source of air contamination at the start of the experiment is incompletely degassed water. We had verified that the headspace pressure was equal to the vapor pressure of water (24.9 ± 1.6 mbar) before each experiment, so the total contaminant from this source was negligible.

Air leaks through vacuum fittings during the experiment may also have affected $\delta^{18}O$ values of the headspace O_2. Indeed, we observed small argon peaks during gas chromatography purification of the latter samples, consistent with the hypothesis of air leaking into the Kimax flask. The integrated area of argon on the GC suggests that the total contribution from air-O_2 was ~1.4% of the headspace O_2, or −0.04‰ in $\delta^{18}O$, during the longest experiment. That experiment had the largest $\delta^{18}O$ offset at the end (−0.11‰), while the shorter second and third experiments had smaller offsets (−0.05‰ and − 0.09‰). This effect may also have been important for the Knox et al. (1992) study, in which the experiment lasted > 400 h and showed a $\delta^{18}O$ offset > 0.1‰ at 100% O_2 saturation.

A third possible source of error is the removal of headspace O_2 during the experiment for analysis. It yields two possible errors. The first error arises from the sampling-induced decrease in the headspace volume of ~30 ml (~60 ml for experiment 1 because the headspace was inadvertently expanded into a larger volume just before sampling the last two samples) over the course of an experiment. This decrease in headspace volume alters the partitioning of O_2 between the dissolved and gas phase—a larger proportion of the total O_2 remaining is dissolved—resulting in a $\delta^{18}O$ change of about −0.02‰ (−0.04‰ for experiment 1) at equilibrium. Samples collected at early stages of the experiments are affected less. The second error arises from the removal of kinetically fractionated gas from the system when the $\delta^{18}O$ of the headspace is higher than 0‰. If all the O_2 removed has $\delta^{18}O_{removed} = 0.2‰$, the maximally fractionated gas in the experiment, and the initial headspace is ~450 mL, the total change in $\delta^{18}O$ for that system would be −0.014‰ (−0.030‰ for experiment 1). Note that this is an extreme case because $\delta^{18}O_{removed} \leq 0.2‰$ under most conditions.

The fourth possible source of error is an inaccuracy in the temperature during the experiment. Temperature changes would affect the concentration of O_2 in the dissolved phase. The maximum variance of temperature during the experiment is < 2 °C (i.e., the temperature was 22 ± 1 °C), which results in an uncertainty of ± 2% in solubility and ± 0.005‰ in $\delta^{18}O$ values. The temperature inaccuracy would be manifest on the saturation plot because the saturation state is calculated according to the measured temperature. The final saturation values were within 3.5% of 100%, which is similar to the expected accuracy. Temperature may have affected the gas transfer rate k_L, but its effects were small compared to those of the water-mixing rate.

We estimate that the cumulative $\delta^{18}O$ offset at 100% O_2 saturation due to all four of the effects described above is −0.086‰ (−0.121‰ for experiment 1), which can explain the offset observed. We also calculated the expected cumulative offsets due to the four effects described above for $^{17}\Delta$, Δ_{36}, and Δ_{35} values. The maximum deviation in $\delta^{18}O$ for

the whole experiment is −0.11‰ which implies a 3.4% air contamination according to Eq. (24). The $^{17}\Delta$ value for air is −100 ppm relative to the working gas, whereas the Δ_{36} and Δ_{35} values for air are about 0.64‰, and 0.3‰ higher than that for air, respectively. By substituting $^{17}\Delta$, Δ_{36}, or Δ_{35} into Eq. (24)—which is a sufficiently accurate approximation of the true mixing relationship in this case—we obtain deviations of –3 ppm, 0.02‰, and 0.01‰ in the $^{17}\Delta$, Δ_{36}, and Δ_{35} values, respectively. These deviations are not detectable based on our long-term external precision. Air contaminants similar in magnitude to the one observed would not result in a detectable offset in those values.

Consequently, the main uncertainty arising from the $\delta^{18}O$ offset is in the $^{34}\alpha_k$ value. Yet, most data points still show good agreement with the model: the high-saturation points (those in the equilibrium-dominated regime) are the most affected, while the low-saturation points (those in the kinetically controlled regime) were less affected. The sampling density was highest in the low-saturation region, so the $^{34}\alpha_k$ value is likely robust.

4. Discussion

4.1. Kinetic fractionation factors of O_2 isotopologues

Our mean measured $^{34}\alpha_k$ value is 0.9978 ± 0.0004 (1σ), which is not significantly different (using $p = 0.05$) from the value determined by Knox et al. (1992), $^{34}\alpha_k$ = 0.9972 ± 0.0002 (1σ). The mean $\theta_{17/18,k}$ value of 0.517 ± 0.002 (1σ) falls in a reasonable range for mass dependent fractionation (Young et al., 2002). It is also consistent with the estimated value of ~0.510 invoked by Yeung et al. (2015) to explain bulk-isotope variations coming from gas transfer in a terrarium experiment. However, that value had been inferred from a biogeochemical model of the terrarium and was not a direct measurement. The mean $\theta_{36/34,k}$ value of 1.948 ± 0.032 is different from the estimated value of ~3.2 suggested by Yeung et al. (2015) to explain bulk-isotope variations in a terrarium experiment, but the latter may have been affected by instrumental artifacts (see Section 4.2). Although we were unable to find a best-fit $\theta_{35/34}$ value from the data, the lack of change in Δ_{35} values during gas exchange (Fig. 4D) suggests that the kinetic fractionation of $^{17}O^{18}O$ during air-water gas transfer yields a $\theta_{35/34}$ value close to 1.5. Taken together, these data provide insight into the mass-dependent fractionation mechanism during gas transfer across the air-water interface.

To understand the physical origin of these $\theta_{kinetic}$ values, one can compare the experimental $\theta_{17/18,k}$ and $\theta_{36/34,k}$ values with mass-dependent fractionation factors for pinhole diffusion and gas-phase O_2 diffusion (inter-diffusion) in pure water vapor. The $\theta_{17/18}$ and $\theta_{36/34}$ values for these two processes are 0.509 and 1.943 for pinhole diffusion and 0.514 and 1.907 for inter-diffusion, respectively (Eq. (14)), calculated using $\alpha_{1/2} = (m_2/m_1)^{1/2}$ and $\alpha_{1/2} = (\mu_2/\mu_1)^{1/2}$, respectively, where μ is the reduced mass of O_2 and a water molecule, i.e. $\mu = m_{O2}m_{H2O}/(m_{O2} + m_{H2O})$. As the number of water molecules increases [e.g., $\mu_{O2\text{-}H2O} = m_{O2} \times 8m_{H2O}/(m_{O2} + 8m_{H2O})$ for an 8-water hydration shell], the $\theta_{17/18}$ and $\theta_{36/34}$ values trend from 0.514 and 1.907 toward 0.509 and 1.943, respectively, i.e., from the inter-diffusion to pinhole-diffusion limits.

The measured $\theta_{17/18,k}$ and $\theta_{36/34,k}$ values for air-water gas transfer—0.517 ± 0.002 and 1.948 ± 0.032 (1σ), respectively—are close to theoretical $\theta_{17/18}$ and $\theta_{36/34}$ values for gas-phase O_2 diffusion in water vapor, but they do not unequivocally reflect pinhole- or inter-diffusion mass dependence. The kinetic $\theta_{17/18}$ value is indistinguishable from the inter-diffusion $\theta_{17/18}$ value, but it is > 2σ different from that for pinhole diffusion. Moreover, the Monte Carlo results (Fig. 5) show fewer than 5% of the best-fit kinetic $\theta_{17/18}$ values being ≤0.509. In contrast, a large proportion of the best-fit kinetic $\theta_{36/34}$ values lie near 1.907. Note also that the $\theta_{36/34,k}$ value for air-water gas transfer depends on the assumed value for $\theta_{36/34,eq}$ at solubility equilibrium. If $\theta_{36/34,eq} < 2$—which the experiments cannot not rule out (see Section 3.1)—then the $\theta_{36/34,k}$ value for air-water gas transfer would be lower than the reported mean value of 1.948. In both cases, the data are more consistent with an inter-diffusion mass dependence than a pinhole-diffusion mass dependence being the rate-limiting step in air-water gas transfer (Jähne and Haußecker, 1998).

4.2. Explaining the unusual clumped-isotope fractionation in the Yeung et al. (2015) dark incubation experiments

Yeung et al. (2015) presented a clumped-isotope analysis of headspace O_2 in a closed-system terrarium experiment. During the dark respiration period, they observed a rapid increase in both Δ_{36} and Δ_{35} values that they hypothesized could arise from kinetic gas-transfer fractionation with apparent $\theta_{36/34}$ and $\theta_{35/34}$ values of 3.2 and 1.8, respectively. The hypothesized kinetic $\theta_{36/34}$ and $\theta_{35/34}$ values are non-mass-dependent, being significantly different from 2.0 and 1.5, respectively. Our experiments show only subtle kinetic effects for $^{18}O^{18}O$ and $^{17}O^{18}O$ beyond those expected for mass-dependent fractionation ($\theta_{36/34}$ = 1.948 ± 0.032 and $\theta_{35/34} \approx 1.5$; Fig. 4C and D). The Δ_{36} and Δ_{35} signals in the terrarium incubation experiment therefore did not arise from gas-transfer fractionation. Unusual clumped-isotopologue fractionation during respiration cannot be ruled out as a factor, however, and awaits further testing. Analytical artifacts could also have contributed to the apparent non-mass-dependent fractionation in the Yeung et al. (2015) terrarium experiment. An empirical ion correction at mass 36 was used in those analyses because the IRMS was unable to resolve $^{18}O^{18}O$ (35.9983 amu) from its isobar ^{36}Ar (35.9676 amu) and $H^{35}Cl$ (35.9767 amu). The correction was performed by peak-hopping to mass 40 and assuming a constant $^{40}Ar/^{36}Ar$ ratio and constant $H^{35}Cl$. Variations in ^{35}Cl and $H^{35}Cl$ ion currents could have affected the measurement of both Δ_{36} and Δ_{35} values in the earlier experiments. We note these corrections were not necessary on the high-resolution IRMS used in this study (Yeung et al., 2016).

4.3. Effect of kinetic gas-transfer fractionation on GOP estimates

The triple oxygen isotope composition of dissolved O_2 in the oceanic mixed layer has been widely used for determining the gross oxygen productivity (GOP) (Luz and Barkan, 2000, 2005, 2009; Hendricks et al., 2004; Juranek and Quay, 2005, 2010, 2013; Sarma et al., 2005; Reuer et al., 2007; Quay et al., 2010; Kaiser, 2011; Prokopenko et al., 2011; Munro et al., 2013; Nicholson et al., 2014; Palevsky et al., 2016; Haskell et al., 2016). However, kinetic gas-transfer effects on these estimates have not yet been determined in part because the $\theta_{17/18,k}$ value had not been measured before this study. Most of the surface ocean is out of solubility equilibrium for O_2 by several percent, so kinetic gas-transfer fractionation could be important. In particular, portions of the Southern Ocean are undersaturated with respect to O_2 on an annual-mean basis (Fig. 1), and it is a key region for the oceanic biological carbon "pump" on glacial-interglacial timescales (Sigman and Boyle, 2000).

A kinetic isotopic effect-enabled box model for the mixed layer was first derived by Kaiser (2011). Below, we present the model using the notation of Prokopenko et al. (2011):

$$h\frac{d([O_2])}{dt} = G - R - k([O_2] - [O_2]_{eq}) \quad (25)$$

$$h\frac{d([O_2]^*X_{dis})}{dt} = G^*X_p - R\alpha_{res}{}^*X_{dis} - k\alpha_k([O_2]^*X_{dis} - [O_2]_{eq}{}^*X_{eq}) \quad (26)$$

In Eq. (25), h is the depth of mixed layer, $d([O_2])/dt$ is the change in dissolved O_2 concentration through time, G and R are the gross photosynthesis and respiration rates in the mixed layer, respectively. The third term, $k([O_2]–[O_2]_{eq})$, is the gas-transfer term in which k is the

piston velocity and $[O_2]–[O_2]_{eq}$ is the extent of O_2 solubility disequilibrium in the mixed layer. Eq. (26) describes the isotopologue-specific concentration change through time using the term $^*X$ to quantify the relative concentration of each minor isotopologue $^*O_2$:

$$^*X = \frac{[^*O_2]}{[^{32}O_2]} \tag{27}$$

corresponding to O_2 produced by photosynthesis (X_p), the O_2 dissolved in that water sample (X_{dis}), and O_2 at solubility equilibrium in the local environment (X_{eq}). On the right side of Eq. (26), GX_p and $R\alpha_{res}X_{dis}$ characterize the photosynthetic and respiratory fluxes of O_2 isotopologues, respectively, relative to the flux of the major O_2 isotopologue ($^{16}O^{16}O$ comprises 99.5% of all O_2, so the model assumes that the total O_2 flux is the same as the $^{16}O^{16}O$ flux). The respiration and gas-transfer terms include respective fractionation factors α_{res} and α_k to represent the dependence of their rates on isotopologue. The kinetic α_k term is the only modification from the Prokopenko et al. (2011) steady-state model.

If the mixed layer is in a steady state for both O_2 concentration and O_2 isotopologues (i.e., $d([O_2])/dt = 0$ and $d([O_2]X_{dis})/dt = 0$), then Eqs. (25) and (26) simplify to:

$$\frac{G}{k[O_2]_{eq}} = \frac{F_1 - 0.518F_2 + (0.518 - 1)\left(\frac{[O_2]}{[O_2]_{eq}} - 1\right)}{F_3 - 0.518F_4} \tag{28}$$

where

$$F_1 = {}^{18}\alpha_k^{\theta_{17/18,k}} * \left(\frac{[O_2]}{[O_2]_{eq}} - \frac{\delta^{17}O_{eq} * 10^{-3} + 1}{\delta^{17}O * 10^{-3} + 1}\right) \tag{29}$$

$$F_2 = {}^{18}\alpha_k * \left(\frac{[O_2]}{[O_2]_{eq}} - \frac{\delta^{18}O_{eq} * 10^{-3} + 1}{\delta^{18}O * 10^{-3} + 1}\right) \tag{30}$$

$$F_3 = \frac{\delta^{17}O_{GOP} * 10^{-3} + 1}{\delta^{17}O * 10^{-3} + 1} - 1 \tag{31}$$

$$F_4 = \frac{\delta^{18}O_{GOP} * 10^{-3} + 1}{\delta^{18}O * 10^{-3} + 1} - 1 \tag{32}$$

These equations are similar to those in Prokopenko et al. (2011), except with kinetic fractionation terms included in the expressions for F_1 and F_2. We note that Eq. (28) is similar to Eq. (1) in the paper of Kaiser and Abe (2012), which has a different preferred notation. All the terms in Eqs. (28)–(32) can be measured in the mixed layer or have been measured in the lab; the terms without subscripts are measured in the mixed-layer's O_2.

To evaluate potential effects of kinetic gas-transfer fractionation on open-ocean estimates of GOP, we used the triple-isotope dataset from the Southern Ocean reported in Reuer et al. (2007). Because the authors did not report the O_2 saturation state, we assumed an Ar saturation state in this region of 95%, which, when combined with their reported $\delta O_2/Ar$ values, yields an O_2 saturation state similar to the annually-averaged range in this region (i.e., 90%–100%). We then compared the relative error in GOP incurred for several values of $\theta_{17/18,\,k}$ (Fig. 6). We evaluated the effects of kinetic gas transfer for three values of $\theta_{17/18,\,k}$: 0.517, the mean experimental value; 0.520, the highest measured value; and 0.514, the lowest measured value.

The calculation shows that kinetic gas-transfer fractionation of isotopologues can have a significant impact on GOP estimates, but only when GOP is low. When GOP is high, the error is generally small (< 5%). When GOP is low (e.g., GOP < 50 mmol O_2 m^{-2} d^{-1}), the error incurred can be up to ± 50% in this dataset; however, most data points are within ± 10% of the GOP calculated if kinetic gas-exchange fractionation is omitted, with a maximum observed inaccuracy of 12 mmol O_2 m^{-2} d^{-1}. Evidently, the large relative errors for low GOP are driven by the small magnitude of triple-isotope signals when GOP is close to zero. This result highlights not the importance of kinetic gas-exchange fractionation, but instead the difficulty in measuring GOP in low-productivity regions, which can also be biased by entrainment of thermocline waters (Nicholson et al., 2012) or errors in bulk gas transfer rates (Ho et al., 2006).

The Southern Ocean is an extreme case with respect to dissolved oxygen saturation, so we expect triple-isotope-based GOP errors arising from omitting kinetic gas-exchange fractionation to be even smaller in most open-ocean environments. In some estuaries and coastal environments, O_2 can be strongly supersaturated, however, so GOP determinations in those contexts may require an explicit treatment of O_2 kinetic fractionation across the air-water interface (Manning, 2017).

4.4. Potential implications for respiration under diffusion limitation

Both theory and the isotopic data suggest that the rate-limiting step for O_2 gas transfer across the air-water interface is diffusion across the aqueous boundary layer (Jähne and Haußecker, 1998). Consequently, kinetic fractionation across the air-water interface can be connected to diffusive fractionation in the dissolved phase.

Diffusive fractionation is important in marine communities that are endemic to sediments and in particles, where the fractionation of isotopes is determined by both diffusion and respiration. One can use a "community" fractionation factor to represent the overall effect of these mechanisms. For a benthic environment (treated as a semi-infinite slab), it can be shown that the O_2 concentration profile inside the slab follows an exponential decay below the sediment-water interface. The fractionation factor for this process equals (Bender, 1990):

$$^{34}\alpha_c = \left(\frac{^{34}k\,^{34}D}{^{32}k\,^{32}D}\right)^{1/2} \tag{33}$$

where k is the respiration rate and D is the diffusion coefficient for different dissolved O_2 isotopologues. The kinetic fractionation due to microbial O_2 consumption is $^{34}\alpha_r = {}^{34}k/{}^{32}k \approx 0.982$ (Schleser, 1979; Bender, 1990), while the kinetic fractionation due to diffusion is the ratio of coefficients, $^{34}\alpha_D = {}^{34}D/{}^{32}D$. The ratio of diffusion coefficients is related to the kinetic gas transfer fractionation via Eq. (11). In our experiment, we observed no visible waves, so the exponent may be closer to 2/3 (limit of perfectly smooth surface) than ½ (rough surface), i.e.,

$$^{34}\alpha_k = \left(\frac{^{34}D}{^{32}D}\right)^{\frac{2}{3}} \tag{34}$$

Using this relationship, we calculate a community fractionation factor of $^{34}\alpha_c = 0.989$ for exponents of 2/3 and 1/2. The results for the other isotopologues are shown in Table 3.

Kinetic fractionation from diffusion, community fractionation, and respiration fractionation are all important in the aphotic zone. Depending on whether respiration is diffusion-limited, the expression of these fractionation factors could be variable; in the case of ^{18}O fractionation, the total range of variability is a factor of two. The θ values may be more constant. Mixing, however, is also important for the O_2 budget (Bender, 1990; Levine et al., 2009). Complementary analysis of $^{17}\Delta$, Δ_{36}, and $\Delta_{35\ 36}$ values in the aphotic zone, which reflect the same contributions from diffusion, respiration, and mixing, may provide the needed additional constraints on these processes in the dark ocean.

5. Conclusions

We present the first experimental determinations of the kinetic isotopic fractionation factors for $^{16}O^{17}O$, $^{17}O^{18}O$, and $^{18}O^{18}O$ relative to $^{16}O^{16}O$ during air-water gas transfer, as well as the equilibrium solubility isotopic fractionation factor for $^{17}O^{18}O$ and $^{18}O^{18}O$ relative to $^{16}O^{16}O$. We also re-determined the kinetic $^{16}O^{18}O/^{16}O^{16}O$ fractionation factor for air-water gas transfer, quantified as a $^{34}\alpha_k$ value, which agrees with the previous determination by Knox et al. (1992). The

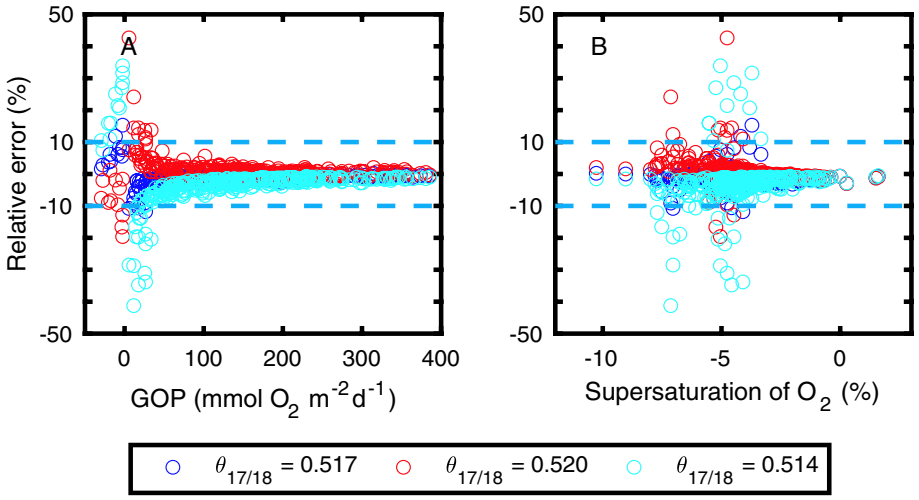

Fig. 6. Potential effects from O_2 solubility disequilibrium on Southern-Ocean GOP estimated using data reported by Reuer et al. (2007). Relative error is defined as $(GOP_{Kinetic}/GOP_{Without\_Kinetic} - 1) * 100\%$. The dashed lines show bounds of ± 10% relative error. Plots show relative error in GOP as a function of (A) GOP and (B) O_2 saturation.

Table 3
Fractionation factors relevant to dissolved O_2 and calculated relationships between $^{16}O^{17}O$, $^{16}O^{18}O$, and $^{18}O^{18}O$ in the aphotic zone (n = 2/3).

Factors	Diffusion	Respiration	Community
$^{33}\alpha$	0.9983	0.991	0.994
$^{34}\alpha$	0.9968	0.982	0.989
$^{36}\alpha$	0.9937	–	–
$\theta_{17/18,\ k}$	0.517	0.518	0.518
$\theta_{36/34,\ k}$	1.948	–	–
$\theta_{17/18,\ theory}$[a]	0.514	0.518	0.518
$\theta_{36/34,\ theory}$[a]	1.907	–	–

[a] Diffusive mass dependence calculated for interdiffusion of O_2 through water vapor. Respiratory mass dependence from Luz and Barkan (2011).

results suggest that kinetic gas transfer likely has negligible effects on GOP in the open ocean. However, in areas of low GOP, analytical uncertainties and uncertainties in gas-transfer rate dominate the uncertainties in GOP estimates. The results may be applicable to the study of O_2 in the deep ocean, where diffusion, respiration, and mixing render the budget difficult to constrain uniquely. Finally, these data will support fundamental theoretical studies of diffusive fractionation in the liquid phase, for which experimental data on the mass dependence of diffusion for diatomic molecules has been lacking.

Supplementary data to this article can be found online at https://doi.org/10.1016/j.marchem.2019.02.006.

Acknowledgements

We would like to thank Justin Hayles, Sizhuang Deng, Ao Cai and Yen Sun for discussions related to modeling and Jan Kaiser and two anonymous reviewers for detailed reviews that greatly improved the paper. This research was supported by the National Science Foundation (OCE-1533501).

References

Angert, A., Rachmilevitch, S., Barkan, E., Luz, B., 2003. Effects of photorespiration, the cytochrome pathway, and the alternative pathway on the triple isotopic composition of atmospheric O_2. Glob. Biogeochem. Cycles 17 (1). https://doi.org/10.1029/2002GB001933.

Bender, M.L., 1990. The $\delta^{18}O$ of dissolved O_2 in seawater: a unique tracer of circulation and respiration in the deep sea. J. Geophys. Res. Oceans 95 (C12), 22243–22252. https://doi.org/10.1029/JC095iC12p22243.

Bender, M.L., 2000. Tracer from the sky. Science 288 (5473), 1977–1978. https://doi.org/10.1126/science.288.5473.1977.

Benson, B.B., Krause, D., 1984. The concentration and isotopic fractionation of oxygen dissolved in freshwater and seawater in equilibrium with the atmosphere1. Limnol. Oceanogr. 29 (3), 620–632. https://doi.org/10.4319/lo.1984.29.3.0620.

Bianchi, D., Weber, T.S., Kiko, R., Deutsch, C., 2018. Global niche of marine anaerobic metabolisms expanded by particle microenvironments. Nat. Geosci. 11 (4), 263–268. https://doi.org/10.1038/s41561-018-0081-0.

Bourg, I.C., Sposito, G., 2008. Isotopic fractionation of noble gases by diffusion in liquid water: molecular dynamics simulations and hydrologic applications. Geochim. Cosmochim. Acta 72 (9), 2237–2247. https://doi.org/10.1016/j.gca.2008.02.012.

Buesseler, K.O., Boyd, P.W., 2009. Shedding light on processes that control particle export and flux attenuation in the twilight zone of the open ocean. Limnol. Oceanogr. 54 (4), 1210–1232. https://doi.org/10.4319/lo.2009.54.4.1210.

Devol, A.H., Hartnett, H.E., 2001. Role of the oxygen-deficient zone in transfer of organic carbon to the deep ocean. Limnol. Oceanogr. 46 (7), 1684–1690. https://doi.org/10.4319/lo.2001.46.7.1684.

Froelich, P. N., Klinkhammer, G. P., Bender, M. L., Luedtke, N. A., Heath, G. R., Cullen, D., et al. (1979). Early oxidation of organic matter in pelagic sediments of the eastern equatorial Atlantic: suhoxic diagenesis, 16.

Garcia, H.E., Gordon, L.I., 1992. Oxygen solubility in seawater: better fitting equations. Limnol. Oceanogr. 37 (6), 1307–1312. https://doi.org/10.4319/lo.1992.37.6.1307.

Gruber, N., Sarmiento, J.L., 1997. Global patterns of marine nitrogen fixation and denitrification. Glob. Biogeochem. Cycles 11 (2), 235–266. https://doi.org/10.1029/97GB00077.

Haskell, W.Z., Prokopenko, M.G., Stanley, R.H.R., Knapp, A.N., 2016. Estimates of vertical turbulent mixing used to determine a vertical gradient in net and gross oxygen production in the oligotrophic South Pacific Gyre. Geophys. Res. Lett. 43 (14). https://doi.org/10.1002/2016GL069523. 2016GL069523.

Helman, Y., 2005. Fractionation of the three stable oxygen isotopes by oxygen-producing and oxygen-consuming reactions in photosynthetic organisms. Plant Physiol. 138 (4), 2292–2298. https://doi.org/10.1104/pp.105.063768.

Hendricks, M.B., Bender, M.L., Barnett, B.A., 2004. Net and gross O_2 production in the southern ocean from measurements of biological O_2 saturation and its triple isotope composition. Deep-Sea Res. I Oceanogr. Res. Pap. 51 (11), 1541–1561. https://doi.org/10.1016/j.dsr.2004.06.006.

Ho, D.T., Law, C.S., Smith, M.J., Schlosser, P., Harvey, M., Hill, P., 2006. Measurements of air-sea gas exchange at high wind speeds in the Southern Ocean: implications for global parameterizations. Geophys. Res. Lett. 33 (16). https://doi.org/10.1029/2006GL026817.

Honjo, S., Manganini, S.J., Krishfield, R.A., Francois, R., 2008. Particulate organic carbon fluxes to the ocean interior and factors controlling the biological pump: a synthesis of global sediment trap programs since 1983. Prog. Oceanogr. 76 (3), 217–285. https://doi.org/10.1016/j.pocean.2007.11.003.

Jähne, B., Haußecker, H., 1998. Air-Water Gas Exchange. Annu. Rev. Fluid Mech. 30 (1), 443–468. https://doi.org/10.1146/annurev.fluid.30.1.443.

Juranek, L.W., Quay, P.D., 2005. In vitro and in situ gross primary and net community production in the North Pacific subtropical Gyre using labeled and natural abundance isotopes of dissolved O_2. Glob. Biogeochem. Cycles 19 (3). https://doi.org/10.1029/2004GB002384.

Juranek, L.W., Quay, P.D., 2010. Basin-wide photosynthetic production rates in the subtropical and tropical Pacific Ocean determined from dissolved oxygen isotope ratio measurements: Pacific basin productivity from O_2 isotopes. Glob. Biogeochem. Cycles 24 (2). https://doi.org/10.1029/2009GB003492.

Juranek, L.W., Quay, P.D., 2013. Using triple isotopes of dissolved oxygen to evaluate global marine productivity. Annu. Rev. Mar. Sci. 5 (1), 503–524. https://doi.org/10.1146/annurev-marine-121211-172430.

Kaiser, J., 2011. Technical note: consistent calculation of aquatic gross production from oxygen triple isotope measurements. Biogeosciences 8 (7), 1793–1811. https://doi.org/10.5194/bg-8-1793-2011.

Kaiser, J., Abe, O., 2012. Reply to Nicholson's comment on “consistent calculation of aquatic gross production from oxygen triple isotope measurements” by Kaiser (2011). Biogeosciences 9, 2921–2933. https://doi.org/10.5194/bg-9-2921-2012.

Kirkwood, D., 1992. Stability of solutions of nutrient salts during storage. Mar. Chem. 38 (3–4), 151–164. https://doi.org/10.1016/0304-4203(92)90032-6.

Knox, M., Quay, P.D., Wilbur, D., 1992. Kinetic isotopic fractionation during air-water gas transfer of O_2, N_2, CH_4, and H_2. J. Geophys. Res. Oceans 97 (C12), 20335–20343. https://doi.org/10.1029/92JC00949.

Levine, N.M., Bender, M.L., Doney, S.C., 2009. The $\delta^{18}O$ of dissolved O_2 as a tracer of mixing and respiration in the mesopelagic ocean. Glob. Biogeochem. Cycles 23 (1). https://doi.org/10.1029/2007GB003162.

Luz, B., Barkan, E., 2000. Assessment of oceanic productivity with the triple-isotope composition of dissolved oxygen. Science 288 (5473), 2028–2031. https://doi.org/10.1126/science.288.5473.2028.

Luz, B., Barkan, E., 2005. The isotopic ratios $^{17}O/^{16}O$ and $^{18}O/^{16}O$ in molecular oxygen and their significance in biogeochemistry. Geochim. Cosmochim. Acta 69 (5), 1099–1110. https://doi.org/10.1016/j.gca.2004.09.001.

Luz, B., Barkan, E., 2009. Net and gross oxygen production from O_2/Ar, $^{17}O/^{16}O$ and $^{18}O/^{16}O$ ratios. Aquat. Microb. Ecol. 56, 133–145. https://doi.org/10.3354/ame01296.

Luz, B., Barkan, E., 2011. Proper estimation of marine gross O_2 production with $^{17}O/^{16}O$ and $^{18}O/^{16}O$ ratios of dissolved O_2. Geophys. Res. Lett. 38 (19). https://doi.org/10.1029/2011GL049138.

Manning, C.C., 2017. Insight into chemical, biological, and physical processes in coastal waters from dissolved oxygen and inert gas tracers. Massachusetts Institute of Technology and Woods Hole Oceanographic Institution, Woods Hole, MA. https://doi.org/10.1575/1912/8589.

Manning, C.C., Howard, E.M., Nicholson, D.P., Ji, B.Y., Sandwith, Z.O., Stanley, R.H.R., 2017. Revising estimates of aquatic gross oxygen production by the triple oxygen isotope method to incorporate the local isotopic composition of water. Geophys. Res. Lett. 44 (20), 10,511–10,519. https://doi.org/10.1002/2017GL074375.

Munro, D.R., Quay, P.D., Juranek, L.W., Goericke, R., 2013. Biological production rates off the Southern California coast estimated from triple O_2 isotopes and O_2: Ar gas ratios. Limnol. Oceanogr. 58 (4), 1312–1328. https://doi.org/10.4319/lo.2013.58.4.1312.

Nicholson, D.P., Stanley, R.H.R., Barkan, E., Karl, D.M., Luz, B., Quay, P.D., Doney, S.D., 2012. Evaluating triple oxygen isotope estimates of gross primary production at the Hawaii Ocean time-series and Bermuda Atlantic time-series study sites. J. Geophys. Res. Oceans 117 (C5). https://doi.org/10.1029/2010JC006856.

Nicholson, D., Stanley, R.H.R., Doney, S.C., 2014. The triple oxygen isotope tracer of primary productivity in a dynamic ocean model: triple oxygen isotopes in a global model. Glob. Biogeochem. Cycles 28 (5), 538–552. https://doi.org/10.1002/2013GB004704.

Palevsky, H.I., Quay, P.D., Lockwood, D.E., Nicholson, D.P., 2016. The annual cycle of gross primary production, net community production, and export efficiency across the North Pacific Ocean. Glob. Biogeochem. Cycles 30 (2). https://doi.org/10.1002/2015GB005318. 2015GB005318.

Prokopenko, M.G., Pauluis, O.M., Granger, J., Yeung, L.Y., 2011. Exact evaluation of gross photosynthetic production from the oxygen triple-isotope composition of O_2: implications for the net-to-gross primary production ratios. Geophys. Res. Lett. 38 (14). https://doi.org/10.1029/2011GL047652.

Quay, P.D., Emerson, S., Wilburn, D.O., Stump, C., Knox, M., 1993. The $\delta^{18}O$ of dissolved O_2 in the surface waters of the subarctic Pacific: a tracer of biological productivity. J. Geophys. Res. Oceans 98 (C5), 8447–8458. https://doi.org/10.1029/92JC03017.

Quay, P.D., Peacock, C., Björkman, K., Karl, D.M., 2010. Measuring primary production rates in the ocean: enigmatic results between incubation and non-incubation methods at station Aloha: primary production rates in the ocean. Glob. Biogeochem. Cycles 24 (3). https://doi.org/10.1029/2009GB003665.

Reuer, M.K., Barnett, B.A., Bender, M.L., Falkowski, P.G., Hendricks, M.B., 2007. New estimates of Southern Ocean biological production rates from O2/Ar ratios and the triple isotope composition of O2. Deep-Sea Res. I Oceanogr. Res. Pap. 54 (6), 951–974. https://doi.org/10.1016/j.dsr.2007.02.007.

Richter, F.M., Mendybaev, R.A., Christensen, J.N., Hutcheon, I.D., Williams, R.W., Sturchio, N.C., Beloso, A.D., 2006. Kinetic isotopic fractionation during diffusion of ionic species in water. Geochim. Cosmochim. Acta 70 (2), 277–289. https://doi.org/10.1016/j.gca.2005.09.016.

Sarma, V.V.S.S., Abe, O., Hashimoto, S., Hinuma, A., Saino, T., 2005. Seasonal variations in triple oxygen isotopes and gross oxygen production in the Sagami Bay, Central Japan. Limnol. Oceanogr. 50 (2), 544–552. https://doi.org/10.4319/lo.2005.50.2.0544.

Schleser, G.H., 1979. Oxygen isotope fractionation during respiration for different temperatures of T. Utilis andE. Coli K12. Radiat. Environ. Biophys. 17 (1), 85–93. https://doi.org/10.1007/BF01323122.

Sigman, D.M., Boyle, E.A., 2000. Glacial/interglacial variations in atmospheric carbon dioxide. Nature 407 (6806), 859–869. https://doi.org/10.1038/35038000.

Stanley, R.H.R., Kirkpatrick, J.B., Cassar, N., Barnett, B.A., Bender, M.L., 2010. Net community production and gross primary production rates in the Western Equatorial Pacific. Glob. Biogeochem. Cycles 24 (4). https://doi.org/10.1029/2009GB003651.

Stramma, L., Prince, E.D., Schmidtko, S., Luo, J., Hoolihan, J.P., Visbeck, M., et al., 2012. Expansion of oxygen minimum zones may reduce available habitat for tropical pelagic fishes. Nat. Clim. Chang. 2 (1), 33–37. https://doi.org/10.1038/nclimate1304.

Tempest, K.E., Emerson, S., 2013. Kinetic isotopic fractionation of argon and neon during air–water gas transfer. Mar. Chem. 153, 39–47. https://doi.org/10.1016/j.marchem.2013.04.002.

Yeung, L.Y., Young, E.D., Schauble, E.A., 2012. Measurements of $^{18}O^{18}O$ and $^{17}O^{18}O$ in the atmosphere and the role of isotope-exchange reactions. J. Geophys. Res. Atmos. 117 (D18). https://doi.org/10.1029/2012JD017992.

Yeung, L.Y., Ash, J.L., Young, E.D., 2015. Biological signatures in clumped isotopes of O_2. Science 348 (6233), 431–434. https://doi.org/10.1126/science.aaa6284.

Yeung, L.Y., Murray, L.T., Ash, J.L., Young, E.D., Boering, K.A., Atlas, E.L., et al., 2016. Isotopic ordering in atmospheric O_2 as a tracer of ozone photochemistry and the tropical atmosphere. J. Geophys. Res. Atmos. 121 (20), 12,541–12,559. https://doi.org/10.1002/2016JD025455.

Yeung, L.Y., Hayles, J.A., Hu, H., Ash, J.L., Sun, T., 2018. Scale distortion from pressure baselines as a source of inaccuracy in triple-isotope measurements. Rapid Commun. Mass Spectrom. 32, 1811–1821. https://doi.org/10.1002/rcm.8247.

Young, E.D., Galy, A., Nagahara, H., 2002. Kinetic and equilibrium mass-dependent isotope fractionation laws in nature and their geochemical and cosmochemical significance. Geochim. Cosmochim. Acta 66 (6), 1095–1104.